Hindawi
Advances in Condensed Matter Physics
Volume 2023, Article ID 8717656, 13 pages
https://doi.org/10.1155/2023/8717656

Research Article

Structural, Electronic, Elastic, Mechanical, and Opto-Electronic Properties for $ZnAg_2SnS_4$ and $ZnAg_2Sn_{0.93}Fe_{0.07}S_4$ Photocatalyst Effort on Wastewater Treatment through the First Principle Study

Mohammad Jahidul Islam,[1,2] **Md. Sabbir Hasan Sohag**,[1] **Unesco Chakma**,[3] **Ajoy Kumer**,[4,5] **Md. Monsur Alam**,[6] **and Mohammed Nazrul Islam Khan**[7]

[1]*Department of Electrical and Electronic Engineering, Bangladesh University of Business and Technology, Mirpur-2, Dhaka-1216, Bangladesh*
[2]*Department of Physics, Jagannath University, Dhaka-1100, Bangladesh*
[3]*Department of Electrical and Electronics Engineering, European University of Bangladesh, Gabtoli, Dhaka-1216, Bangladesh*
[4]*Laboratory of Computational Research for Drug Design and Material Science, Department of Chemistry, European University of Bangladesh, Dhaka-1216, Bangladesh*
[5]*Department of Chemistry, Bangladesh University of Engineering and Technology, Dhaka-1000, Bangladesh*
[6]*Department of Civil Engineering, European University of Bangladesh, Gabtoli, Dhaka-1216, Bangladesh*
[7]*Materials Science Division, Atomic Energy Center, Dhaka, Bangladesh*

Correspondence should be addressed to Mohammad Jahidul Islam; jahidulkhan106490@gmail.com

Received 6 April 2023; Revised 28 May 2023; Accepted 30 May 2023; Published 5 June 2023

Academic Editor: Tholkappiyan Ramachandran

The stannite structured $ZnAg_2SnS_4$ was developed from its parent composition $ZnAg_2GeS4$, which is considered to be an excellent photocatalytic material, as the demands for photocatalytic effect on organic and waste water treatment have been increasing around the globe. First and foremost, the geometry optimization was performed by density functional theory (DFT) of the generalized gradient approximation (GGA) with Perdew–Burke–Ernzerhof (PBE)-ballpark figured as the successful candidate for computational screening containing heavy metal complexes. The structural geometry parameters were determined along with the electronic band structure, density of state (DOS), partial density of state (PDOS), Mulliken charge population, elastic constant, and optical characteristics. When the Ge ($ZnAg_2GeS_4$) atom has been swapped out by a Sn ($ZnAg_2SnS_4$) atom, the changes in band gap is noticeable, which rises from 0.94 eV to 1.15 eV with the same geometry and surface area. But, after 7% Fe doping, it has decreased to 0.32 eV. The PDOS demonstrates that the production of hydrogen for photocatalytic influence on wastewater treatment is dependent on the Fe atom's ability to induce and boost the electron density in both the conduction band and the valence band. The study of the elastic constant and mechanical constant revealed that these crystals are extremely stable in any environment. The dielectric constant and optical absorptions illustrate the superior evidence for photocatalytic activity. To sum up, it could be said that after doping of Fe, the elastic constant and mechanical constant show all universal anisotropic index crystals and $ZnAg_2Sn_{0.93}Fe_{0.07}S_4$ can absorb a variety of UV radiation, which raises the possibility that it could function as a photocatalyst.

1. Introduction

For the last two decades, the photocatalytic degradation process has been used as a promising wastewater treatment method for the mitigation of organic wastewater pollutants due to its numerous merits [1]. As water contamination has inauspicious effects on both human living life and ecosystems, it is a drastic biodegradable problem and impossible to avoid the water pollution system or even stop this industrialization, a major source of water pollution and the backbone of the modern civilization of every country. This issue has become a pressing problem in certain countries, including Bangladesh, India, Pakistan, China, Indonesia, and some African nation, where a number of industries, including those producing ready-to-wear garments, industries, pharmaceuticals, paint industries, and household waste, have been expanding while disregarding the apex of environmental sustainability [2, 3]. Additionally, the human population, as well as the unexpected growth in industry both rise and create the greatest demand for clean water resources, while wastewater is generated by several processes and endangers the quality of these resources. The availability and quality of pure water support sustainable development, human and biodegradation environmental health, and food and energy security [4]. On that account, it is therefore highly imperative that wastewater is adequately managed prior to release from the industry to reduce the ghastly impact on the human body and ecosystems unless it poses threatening and alarming hazard to both developed and developing nation. It is reported that roughly 30% of the naturalistic ambiance has been destroyed after the Second World War, despite the hazardous organic-inorganic contamination has been purified by biological and conventional processes [5, 6]. However, it has been reported that some organic adulterants were not eliminated in these procedures. In this case, the researcher chose photocatalytic and photocatalysis methods as an emerging technique for the mitigation of organic pollutants using a sustainable oxidation process due to its efficiency of photoactivity [7], high stability [8], low cost [9,10], low toxic [11], and safety to human health and environment [12, 13]. Moreover, the oxidation process has a great impact on removing the toxic organic pollutants in wastewater and turning them into carbon dioxide and water. Additionally, its process has several advantages, including quick processing, a simple reaction system, recyclable materials, self-regenerated, non-consumption of oxygen, and producing a high level of UV or visible light absorption [14]. Photocatalytic semiconductors, as well as other optoelectronic devices [15, 16], are employed in the degradation process for many industrial dyes and antibiotics from pharmaceutical and other industries [17–21] because photocatalysis manipulated a variety of fundamental features, including maximum photocatalytic efficiency, a large surface area, light harvesting, reusable, and facilitates the charge carrier separation or enhances the surface reaction of material [22–26]. The method of photocatalysis produces the electron-hole pair due to induced phot-generation, which leads to the production of superoxide free radicals, and by reacting with oxygen, water molecules, and organic pollutants, causes OH, a free radical. Researchers have discovered some photocatalysts for the photocatalytic destruction of pollutants, such as TiO_2, ZnO, $BaTiO_3$, $KNbO_3$, $SrBi_4$, Ti_4O_{15}, and WO_3 [27–31]; these materials can be used to exploit UV or visible light as an endless supply of energy [32]. In general, the following materials can be used in rare-earth (Sm/Nd)-lanthanum ferrite-based perovskite ferroelectric and magnetic nanopowders: AFe2O4 (A = Co, Mg, and Mn) complexes for showing magnetostructural properties; Mn-doped LaFeO3; and nanocrystalline zinc ferrite particles as perovskite materials, which have not been seen to be photocatalytic but have good opto-electric properties [34]. There has been considerable theoretical, experimental, and synthetic research on the probable environmental and energy applications of stannite-type quarterly crystals such as BAg2CX4 (B = Zn, Cd, Pb, Fe, Mn, Hg; C = Si, Ge, Sn; X = S, Se, Te). [37–39]. Metal nanophotocatalysts are easily reusable due to their magnetic function and are strongly associated to organic pollutant mitigation. It is reported that the energy gap value was 2.2 eV for $ZnAg_2GeS_4$ materials did not utilize all the range of visible light in order to achieve a wider band gap [17, 26]. Additionally, $ZnCu_2SnS_4$ semiconductor has been used as an ambiance-friendly photocatalyst as well as a photovoltaic solar cell, and perovskites implications have a straight band gap of 1.5 eV [40–44].

In this work, the new stannite type quarterly crystals, $ZnAg_2SnS_4$, have been designed and investigated their electronic structure and optical properties, and mechanical or electric properties have been calculated which were compared with established photocatalytic $ZnAg_2GeS_4$ materials. Secondly, Fe atom has doped into Sn on $ZnAg_2SnS_4$ and made a comparative study on how the photocatalytic nature can be changed. Next, the optical properties such as conductivity and absorption show how much of light can be absorbed by the materials, that is, the vital factor acting as the photocatalytic behavior even loss function which says how energy or system be suitable for the study. Finally, calculating the elastic properties can give the evidence of molecular and physical stability of designed crystal.

2. Computational Methods

According to the basis principle, generalized gradient approximation (GGA) is more physically consistent than a local-density approximations (LDA), which depends on the gradient of the density, and it is a true exchange-correlation functional of DFT. In addition, the Perdew–Burke–Ernzerhof (PBE) function is very popular because it is a nonempirical function with reasonable accuracy over a wide range of systems. As a result, the PBE techniques were used for optimization for Cu_2ZnSnS_4, and $ZnAg_2GeS_4$ crystal's structure at first [45]. The tetragonal type and space group $I\bar{4}$ were chosen for theoretical calculation since it described identical experimental data in Table 1. As a first step of the process, the electronic structures of $ZnAg_2GeS_4$, $ZnAg_2SnS_4$, and $ZnAg_2Sn_{0.93}Fe_{0.07}S_4$ crystals were calculated using the GGA with PBE method, which was implemented in the CASTEP code [46] in Material Studio 8.0 [47]. For $ZnAg_2GeS_4$ and $ZnAg_2Sn_{0.93}Fe_{0.07}S_4$ simulations, the cutoff was maintained at 523, the k point was fixed at $4 \times 4 \times 2$, and the total energy was set to 1×10^{-5} eV/atom with the norm-conserving pseudopotentials functional. Both the density of states and the optical characteristics were determined under these conditions. After simulation, the elastic stiffness constants of $ZnAg_2SnS_4$ and $ZnAg_2Sn_{0.93}Fe_{0.07}S_4$ at atmospheric pressure by employing the stress-strain technique were calculated. On the other hand, band gap analyzed using GGA and PBE showed that GGA works on all crystals under the similar conditions, which implies that additional study in this area is possible. Finally, for the purpose of forecasting the structural, electrical, elastic, mechanical,

Table 1: Structural calculation by four methods of $ZnAg_2GeS_4$, $ZnAg_2SnS_4$, and $ZnAg_2Sn_{0.93}Fe_{0.07}S_4$.

Compounds	a (Å)	b (Å)	c (Å)	α (°)	β (°)	γ (°)	Crystal type	Space group	Density (g/cm^3)
$ZnAg_2GeS_4$	6.671	6.671	6.671	128.48	128.48	75.849	Tetragonal	I $\bar{4}$	4.52
$ZnAg_2SnS_4$	6.671	6.671	6.671	128.48	128.48	75.849	Tetragonal	I $\bar{4}$	4.52
$ZnAg_2Sn_{0.93}Fe_{0.07}S_4$	6.671	6.671	6.671	128.48	128.48	75.849	Tetragonal	I $\bar{4}$	4.52

and optical properties of $ZnAg_2GeS_4$, $ZnAg_2SnS_4$, and $ZnAg_2Sn_{0.93}Fe_{0.07}S_4$, as depicted in Figures 1(a)–1(c), the $2 \times 1 \times 1$ supercell types were to be accounted.

3. Results and Discussion

3.1. Structural Properties. The lattice parameter values of $ZnAg_2GeS_4$, $ZnAg_2SnS_4$, and $ZnAg_2Sn_{0.93}Fe_{0.07}S_4$ were calculated by the material studio after optimizing their crystal structures, which are listed in Table 1. Furthermore, it should be noted that the optimization structure shown in Figures 1(a)–1(c) was obtained after simulation of GGA with PBE, which has been considered as the standard functional of DFT in the presence of heavy metal atoms in the crystal.

The Mulliken bond populations (P^{μ}) have been utilized to find significant information about the chemical bonding nature of crystal materials in detail. The values of the Mulliken bond populations of $ZnAg_2SnS_4$ and $ZnAg_2Sn_{0.93}Fe_{0.07}S_4$ are listed in Table 2. The bonding and antibonding states are indicated by the negative value and positive value of P^{μ}, respectively. From Table 2, it evidences that all bonds including S-Zn, Ag-S, S-Sn, S-Sn, and Fe-S indicate the boding nature due to the positive value of P^{μ} for both the compounds, $ZnAg_2SnS_4$ and $ZnAg_2Sn_{0.93}Fe_{0.07}S_4$.

3.2. Electronic Structure. The electronic structure has been used to calculate the electronic properties of $ZnAg_2GeS_4$, $ZnAg_2SnS_4$, and $ZnAg_2Sn_{0.93}Fe_{0.07}S_4$. The Fermi level (EF) between the valence and conduction band was indicated at 0 eV. The energy gap between the maximum valence band and the lowest energy state of the conduction band is closely related to the LUMO-HOMO gap [48–51]. The crystal materials have two types of energy bands, either direct or indirect band gaps. In Figures 2(a) and 2(b), it was observed that the momentum of the lowest energy state of the conduction band and maximum valence band was found at the same symmetry point G and it reacts as a direct band gap. Therefore, an electron can shift from the maximum energy state of the valence band to the lowest energy state of the conduction band without altering momentum for both $ZnAg_2GeS_4$ and $ZnAg_2SnS_4$ compounds. The calculated band gap has been observed at 0.93 eV for the $ZnAg_2GeS_4$ crystal. Figure 2(a) shows the electronic band gap, which has been reported to be 1.15 eV for $ZnAg_2SnS_4$ crystal. After doping 7% of Fe atoms, the band started to decrease significantly, which has been recorded at 0.32 eV, as shown in Figure 2(c). It can be observed that this material follows an indirect band gap by revealing minimum conduction band and maximum valence band, which are completely different symmetry points for $ZnAg_2Sn_{0.93}Fe_{0.07}S_4$. The electron cannot readily transit from the greatest energy level of the conduction band to the lowest energy state of the valence band without experiencing a change in momentum because of the indirect band gap. The values of the electronic band gaps for $ZnAg_2GeS_4$, $ZnAg_2SnS_4$, and $ZnAg_2Sn_{0.93}Fe_{0.07}S_4$ semiconductors are listed in Table 3.

3.3. Density of States and Partial Density of States. The density of states plays a crucial role in demonstrating the nature of electronic band structures and the scattering orbitals. The suitable method GGA with PBE has been used to interpret total density of states (TDOS) and partial density of states (PDOS) of Zn, Ag, Sn, Fe, and S atoms for $ZnAg_2SnS_4$ and $ZnAg_2Sn_{0.93}Fe_{0.07}S_4$ compounds. Figure 3(a) depicts the comparative study of TDOS between ZnAg2SnS4 and $ZnAg_2Sn_{0.93}Fe_{0.07}S_4$ crystals. It can be observed that the $ZnAg_2Sn_{0.93}Fe_{0.07}S_4$ crystal has higher electron densities in both the valence and conduction bands compared to $ZnAg_2SnS_4$. Figure 3(b) illustrates the PDOS of $ZnAg_2SnS_4$ which reveals that the nature of s and d orbitals for Zn; s and d for Ag; s, d, and p for Sn; and s and p for S elements have been examined for exploring electron transitions owing to hybridization by transferring from the highest energy state of the valence band to the lowest energy state of the conduction band. From Figures 3(b) and 3(c), it is also observed that robust hybridization is significantly affected by the d orbital in the valence band (VB) and that strong hybridization of the conduction band (CB) is responsible for the s orbital for both $ZnAg_2SnS_4$ and $ZnAg_2Sn_{0.93}Fe_{0.07}S_4$ crystals. Figures 3(d)–3(j) depict the contribution of individual atoms to the production of total density of states (TDOS) and partial density of states (PDOS), with Fe atoms responsible for decreasing the band gap between VB and CB. As can be seen, the Fe atom contributes to higher below-Fermi and above-Fermi energy levels, raising the valence band level while decreasing the conduction band level. For this reason, the band gap was declined by 7% due to Fe atom doping on $ZnAg_2SnS_4$.

3.4. Elastic Constants and Mechanical Properties. A solid's mechanical characteristics and elastic constants, which affect things such as debye temperature, dislocation motion, and stress-strain behavior, are important parameters. In a tetragonal crystal system, there are six independent elastic constants, namely, C_{11}, C_{12}, C_{13}, C_{33}, C_{44}, and C_{66}. Some mechanical and dynamical properties of the material can be determined by its elastic constants. The traditional mechanical stability conditions under isotropic pressure for a tetragonal crystal are given by the following equation:

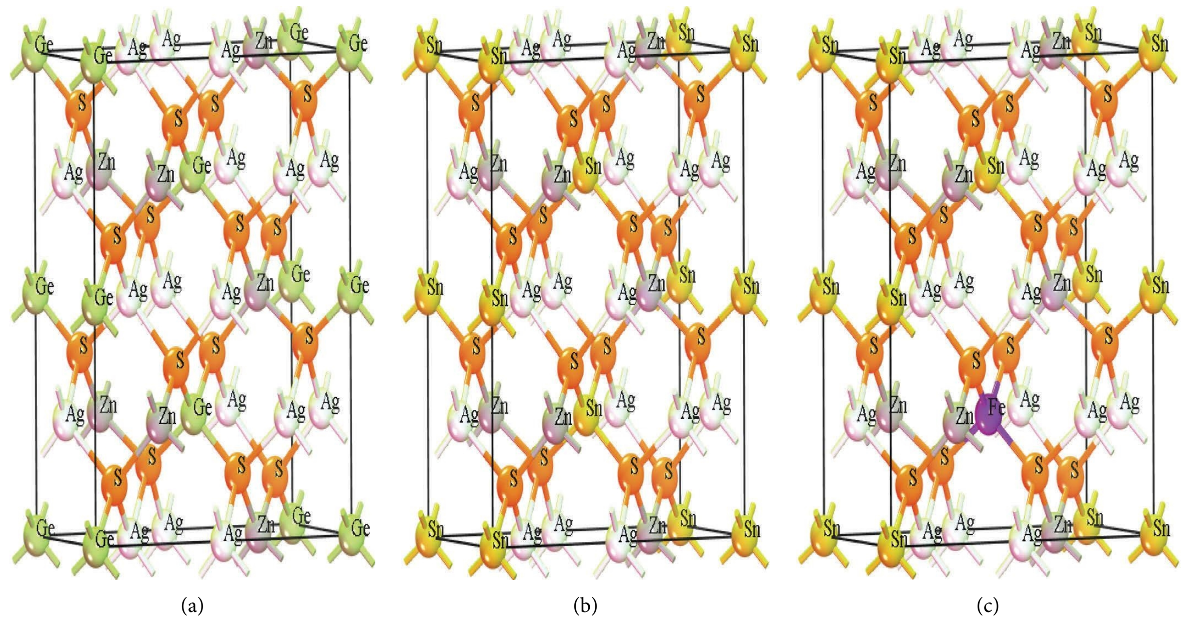

FIGURE 1: Optimized structure of (a) $ZnAg_2GeS_4$, (b) $ZnAg_2SnS_4$, and (c) $ZnAg_2Sn_{0.93}Fe_{0.07}S_4$.

TABLE 2: Mulliken population analysis of $ZnAg_2SnS_4$ and $ZnAg_2Sn_{0.93}Fe_{0.0.07}S_4$ from the GGA method.

	Species	*s*	*p*	*d*	*f*	Total	Charge	Bond	Population	Length
$ZnAg_2SnS_4$	Zn	0.24	0.89	9.98	0.0	11.11	0.89	S-Zn	0.29	2.36
	Ag	2.54	6.42	9.92	0.00	18.87	0.13	Ag-S	0.30	2.55
	Sn	1.26	1.86	9.99	0.00	13.12	0.88	S-Sn	0.64	2.254
	S	1.83	4.66	0.00	0.00	6.49	−0.49	—	—	—
$ZnAg_2Sn_{0.93}Fe_{0.0.07}S_4$	Zn	0.19	0.92	9.97	0.00	11.08	0.92	S-Zn	0.31	2.36
	Ag	2.57	6.51	9.85	0.00	18.94	0.06	Ag-S	0.29	2.55
	Sn	1.28	1.86	9.99	0.00	13.13	0.87	S-Sn	0.65	2.25
	Fe	0.58	0.56	6.72	0.00	7.86	0.14	Fe-S	0.61	2.25
	S	11.85	4.48	0.00	0.00	6.32	−0.32	—	—	—

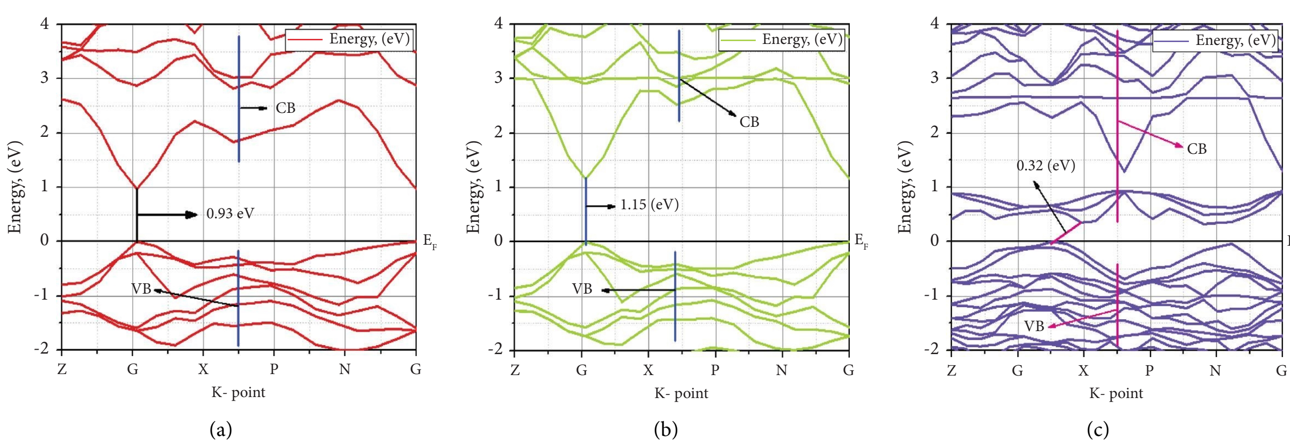

FIGURE 2: Electronic structure of (a) $ZnAg_2GeS_4$, (b) $ZnAg_2SnS_4$, and (c) $ZnAg_2Sn_{0.93}Fe_{0.07}S_4$.

Table 3: Band gap for $ZnAg_2GeS_4$, $ZnAg_2SnS_4$, and $ZnAg_2Sn_{0.93}Fe_{0.07}S_4$.

Crystals/functional	GGA with PBE (eV)	Ref
$ZnAg_2GeS_4$ (parent crystal)	0.93	0.942 eV [17, 26, 52]
Ag_2ZnSnS_4	1.15	Newly predicted
$ZnAg_2Sn_{0.93}Fe_{0.07}S_4$	0.32	Newly predicted

$$C_{11} > 0, C_{33} > 0, C_{44} > 0, C_{66} > 0, C_{11} - C_{12} > 0;$$
$$(C_{33} + C_{11} - 2C_{13}) > 0; \quad (1)$$
$$(2C_{11} + 2C_{12} + C_{33} + 4C_{13}) > 0.$$

Table 4 depicts that the elastic constants are positive for $ZnAg_2SnS_4$ and satisfy all the born stability conditions, which further confirms that it is indeed a mechanically stable material. But, $ZnAg_2Sn_{0.93}Fe_{0.07}S_4$ crystal is elastically unstable due to one of the elastic constants showing negative that does not satisfy born stability criteria. The values of bulk modulus (B) and shear modulus (G) for $ZnAg_2SnS_4$ and $ZnAg_2Sn_{0.93}Fe_{0.07}S_4$ tetragonal crystals have been calculated with the help of elastic constants C_{ij} using the expressions built up by Ghebouli et al. [53] for B and G in their literature and listed in Table 5. From Table 5, it can be seen that $C_{12} < B < C_{11}$ satisfies the bulk modulus criteria for $ZnAg_2SnS_4$ and $ZnAg_2Sn0._{93}Fe_{0.07}S_4$. The values of Young's modulus (E) and Poisson's ratio (n) have been evaluated by using the equation developed by Panda and Ravi Chandran [54] and Ravindran et al. [55] for E and n, respectively. The higher values of Young's modulus for $ZnAg_2SnS_4$ and $ZnAg_2Sn_{0.93}Fe_{0.07}S_4$ depict the stiffer nature. Three different methods have been used to estimate the ductility and brittleness of $ZnAg_2SnS_4$ and $ZnAg_2Sn_{0.93}Fe_{0.07}S_4$ crystal materials, which are related to the method of Cauchy pressure, Pugh's ratio, and Poisson's ratio, respectively. The positive value of CP reveals the ductile and ionic bonding nature of the materials, while the negative indicates the brittle and covalent bonding nature of the materials. The values of Pugh's ratio defined by B/G shows greater than 1.75 which indicates a ductile nature, while values below 1.75 indicate the brittle nature of the compound. Finally, the value of Poisson's ratio above 0.26 depicts the ductile nature of the compound. If it is significantly brittle, it can be said from Table 5 that all three methods suggest the ductile nature of both $ZnAg_2SnS_4$ and $ZnAg_2Sn_{0.93}Fe_{0.07}S_4$ materials. The values of the universal anisotropic index, AU, are not zero, which indicates both materials are anisotropic as listed in Table 5.

3.5. Photocatalytic Activity. As a result of the metal oxide's or metal crystal's catalytic action, the photocatalytic reaction proceeds via oxidation and reduction processes. Negative electrons are responsible for reduction, but positive holes join with water molecules from moisture to generate hydroxyl radicals, which are the byproduct of an oxidative reaction. The operation is described in detail below.

Specifically, electron-hole pairs are activated by UV light. When the photogenerated electrons come into contact with O_2, they form reactive anion radicals, such as O_2^-. Appropriate photon irradiation initiates the creation of photogenerated electron-hole pairs on the photocatalyst surface. Active OH free radicals react with water to form holes, which can subsequently be used to degrade organic pollutants. The hydrogen ions can be converted to hydrogen molecules by photoexcited electrons once they are in the conduction band. The band gap is directly related to the amount of ultraviolet light that can pass through it. Most of the photocatalysts has a band gap of 3.2–2.8 eV, which is approximately 387.45–442.80 nm in wavelength. However, it was found that the excellent photocatalyst corresponds to 688.80 nm wavelengths, indicating a band gap of 1.8 eV or lesser. $ZnAg_2SnS_4$ and $ZnAg_2Sn_{0.93}Fe_{0.07}S_4$ were explored for their 1.15 eV and 0.32 eV band gaps, respectively. Further research has revealed that $ZnAg_2Sn_{0.93}Fe_{0.07}S_4$ can absorb a variety of UV radiation, which raises the possibility that it could function as a photocatalyst.

3.6. Optical Properties. The photocatalyst is dependent on a number of active sites, including light absorption, charge mobility, and the magnitude of band gap and electron-hole transportation in terms of conductivity, reflectivity, refractive index, and loss function. Furthermore, a material with a wide surface area is more effective at absorbing pollutants because it creates a greater number of active surface sites, which in turn speeds up the degradation or oxidation of the pollutant.

3.6.1. Optical Reflectivity. Reflectivity is a significant optical property that describes the amount of light that strikes the surface of the photocatalytic material. This can be examined from the reflectivity data, which is related to the absorbance of that material. In previous research examined, the higher absorption spectrum of UV or visible light indicates a lower reflectivity. Figure 4(a) depicts the reflectivity values of $ZnAg_2SnS_4$ and $ZnAg_2Sn_{0.93}Fe_{0.07}S_4$ that have been observed in the range of photon energy from 0 eV to 5 eV. Initially, the reflectivity value of ZnAg2SnS4 near Fermi energy at 0 eV is around 0.2, whereas the reflectivity of $ZnAg_2Sn_{0.93}Fe_{0.07}S_4$ is about 0.4. The reflectivity value of $ZnAg_2SnS_4$ then gradually increased with rising photon energy and reached about 0.3, while the reflectivity value of $ZnAg_2Sn_{0.93}Fe_{0.07}S_4$ decreased rapidly and reached around 0.2 at 2.7 eV. Because of its lower reflectivity value at higher photon energy, $ZnAg_2Sn_{0.93}Fe_{0.07}S_4$ semiconductor may be a better photocatalytic material compared to $ZnAg_2SnS_4$.

3.6.2. Absorption. The optical spectrum is an impactful process where light energy is converted to other forms of energy depending on the nature of the energy band gap. For direct band gap semiconductors, optical absorption occurs at a higher photon energy than the energy gap (Eg) between VB and CB. The absorption spectrum is modest for indirect band gap semiconductors without exceeding the direct gap

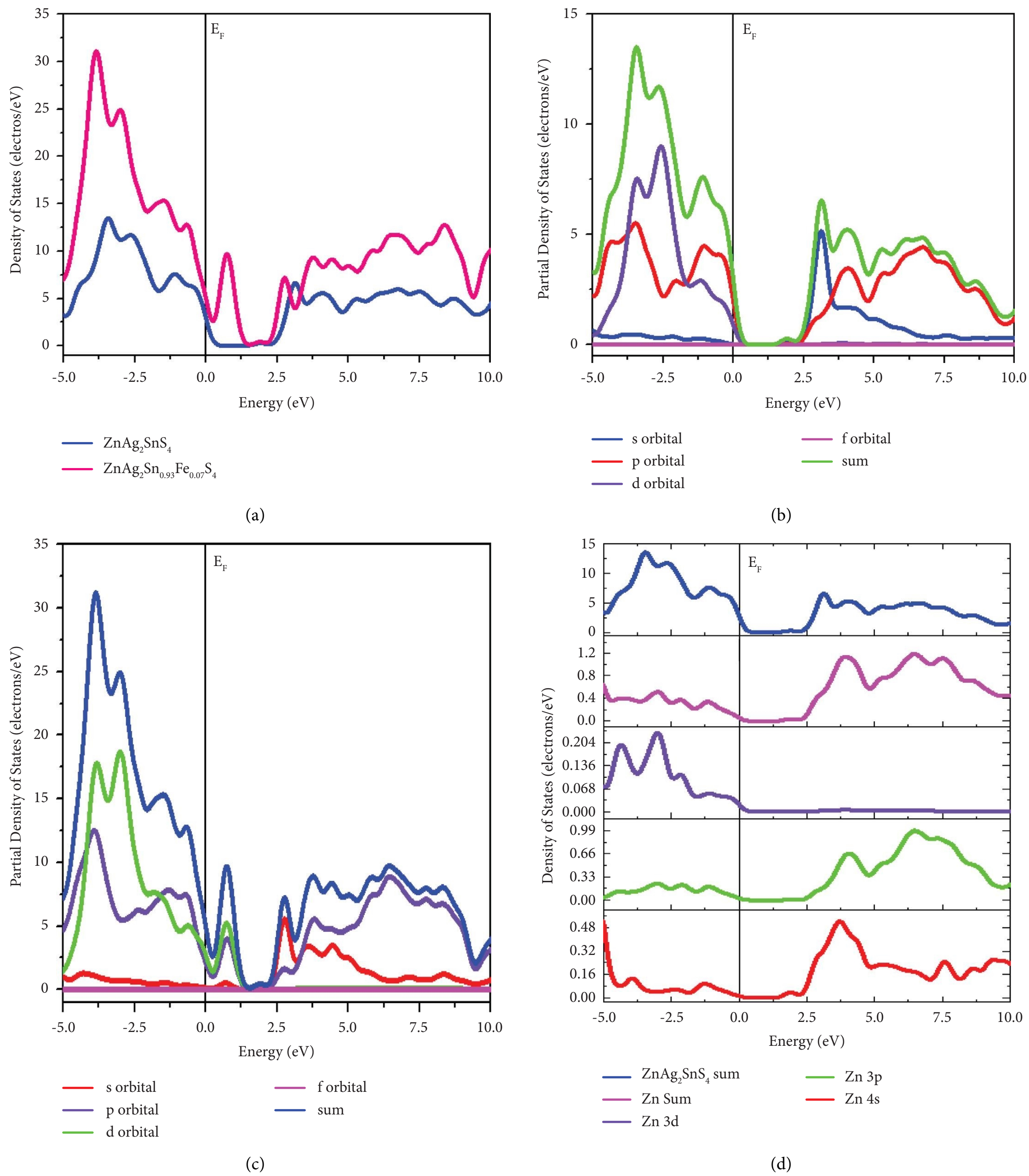

Figure 3: Continued.

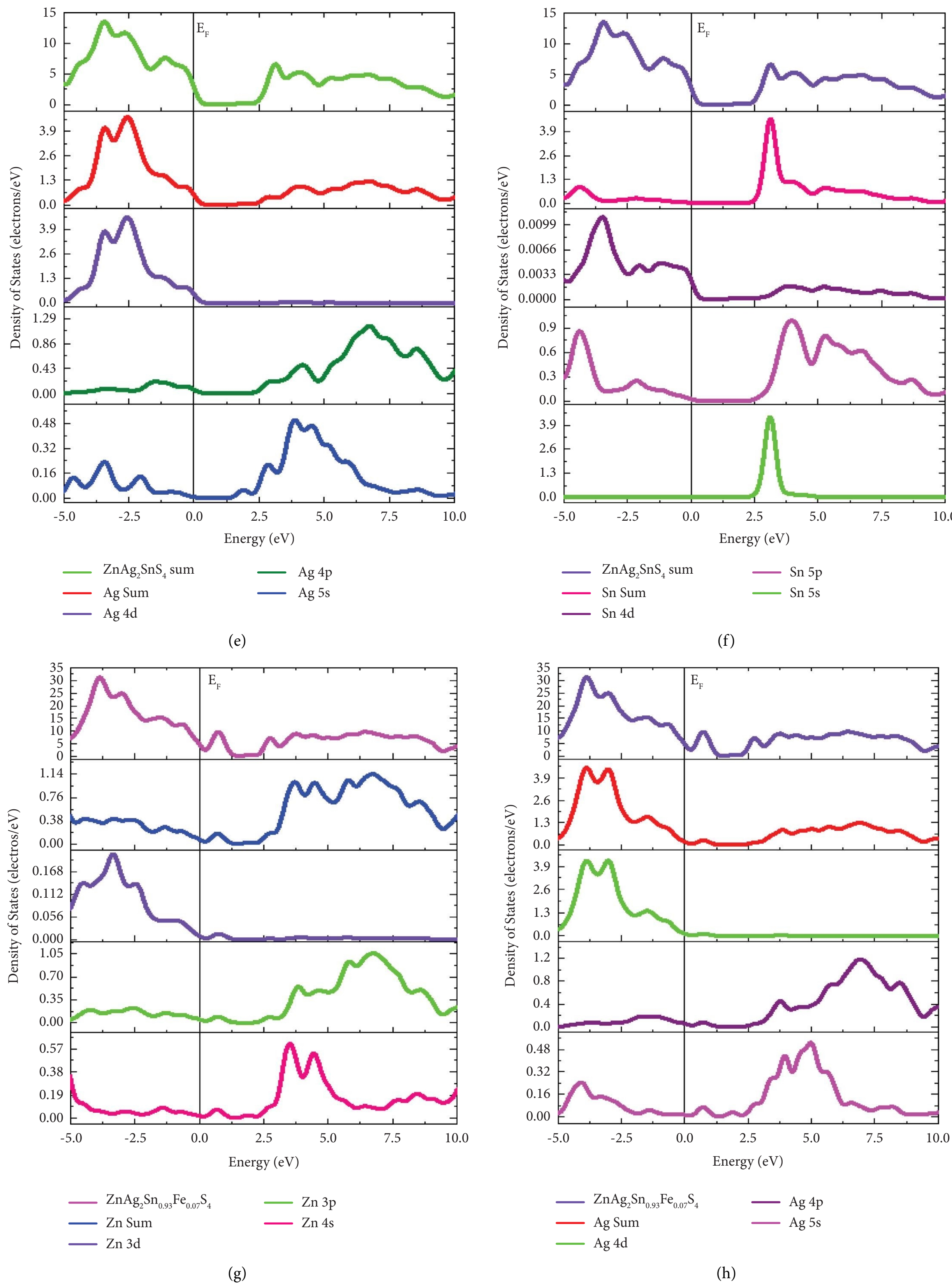

FIGURE 3: Continued.

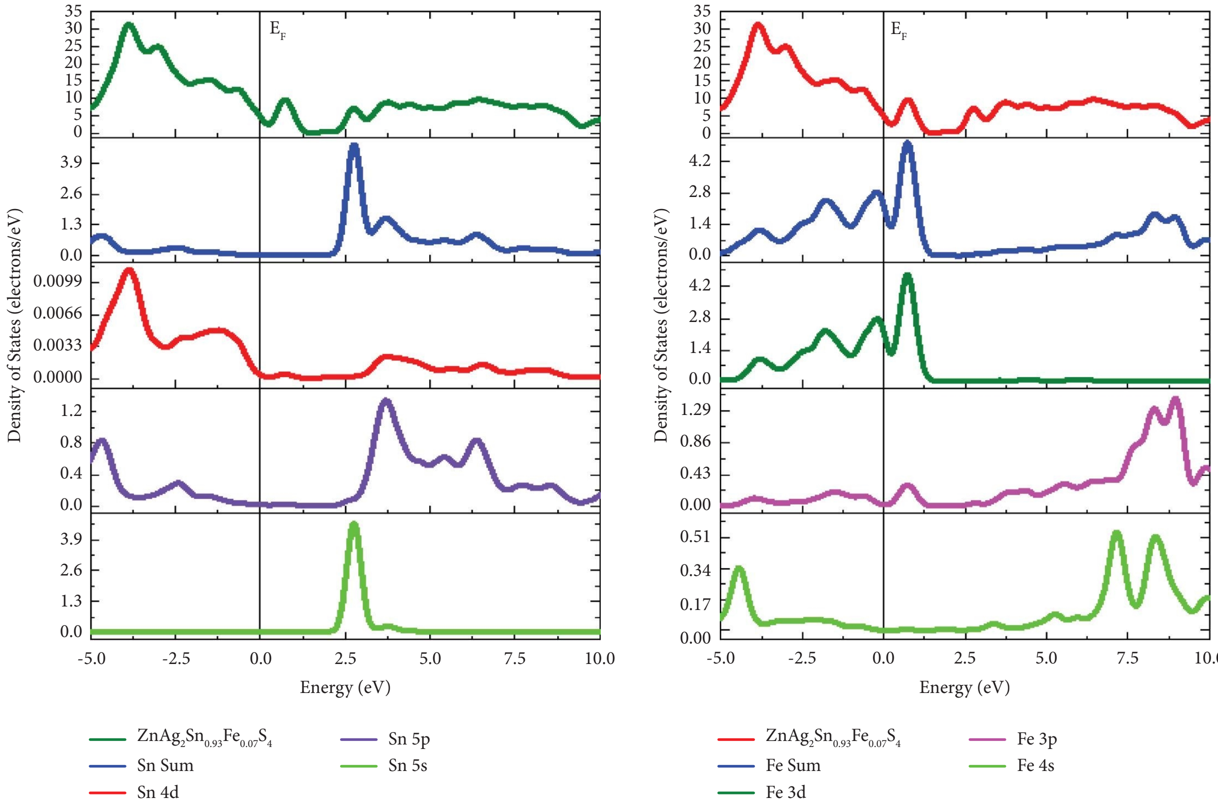

(i) (j)

FIGURE 3: (a) Comparison of the total DOS for $ZnAg_2SnS_4$ and $ZnAg_2Sn_{0.93}Fe_{0.07}S_4$, (b) PDOS for $ZnAg_2SnS_4$, (c) PDOS for $ZnAg_2Sn_{0.93}Fe_{0.07}S_4$, (d) DOS of Zn atom for $ZnAg_2SnS_4$, (e) DOS of Ag atom for $ZnAg_2SnS_4$, (f) DOS of Sn atom for $ZnAg_2SnS_4$, (g) DOS of Zn atom for $ZnAg_2Sn_{0.93}Fe_{0.07}S_4$ (h) DOS of Ag atom for $ZnAg_2Sn_{0.93}Fe_{0.07}S_4$, (i) DOS of Sn atom for $ZnAg_2Sn_{0.93}Fe_{0.07}S_4$, and (j) DOS of Fe atom for $ZnAg_2Sn_{0.93}Fe_{0.07}S_4$.

TABLE 4: Calculation of elastic constants (Cij in GPa), and debye temperature in K.

Compound	C_{11}	C_{12}	C_{44}	C_{13}	C_{33}	C_{66}	Debye temperature, θ_D
$ZnAg_2SnS_4$	85.10	55.50	35.80	58.65	67.03	28.32	235.2
$ZnAg_2Sn_{0.93}Fe_{0.0.07}S_4$	44.97	32.76	−52.17	39.34	47.84	23.47	Elastically unstable

TABLE 5: Calculation of bulk modulus (B in GPa), shear modulus (G in GPa), Cauchy pressure (C_P in GPa), Pugh's ratio (B/G), Young's modulus (E in GPa), Poisson's ratio (n), and universal anisotropic index A^U.

Compound	B	G	C_P	B/G	E	n	A^U
$ZnAg_2SnS_4$	63.55	15.79	19.69	2.66	43.75	0.38	2.72
$ZnAg_2Sn_{0.93}Fe_{0.0.07}S_4$	38.84	9.03	84.93	4.30	25.14	0.39	−12.95

value. The calculated absorption spectrum values of $ZnAg_2SnS_4$ and $ZnAg_2Sn_{0.93}Fe_{0.0.07}S_4$ materials are depicted in Figure 4(b). It is found that absorption peaks are attributed to the transition of energy from the highest energy states of the valence band to the lowest energy state of the conduction band under UV or visible light illumination, which implies that materials can absorb photons in the visible range. In earlier studies, the acceptable photocatalytic material was tested using greater values of absorption peaks. The absorption peaks start from zero near photon energy at 0 eV for both $ZnAg_2SnS_4$ and $ZnAg_2Sn_{0.93}Fe_{0.0.07}S_4$. The absorption of $ZnAg_2Sn_{0.93}Fe_{0.0.07}S_4$ is much higher than $ZnAg_2SnS_4$ within photon energy around 3.5 eV; following that both materials exhibit an essentially identical trend with increasing temperature.

3.6.3. Refractive Index. The index of refraction is an important parameter for defining the characteristics of an optical material that reveals how quick visible light travels

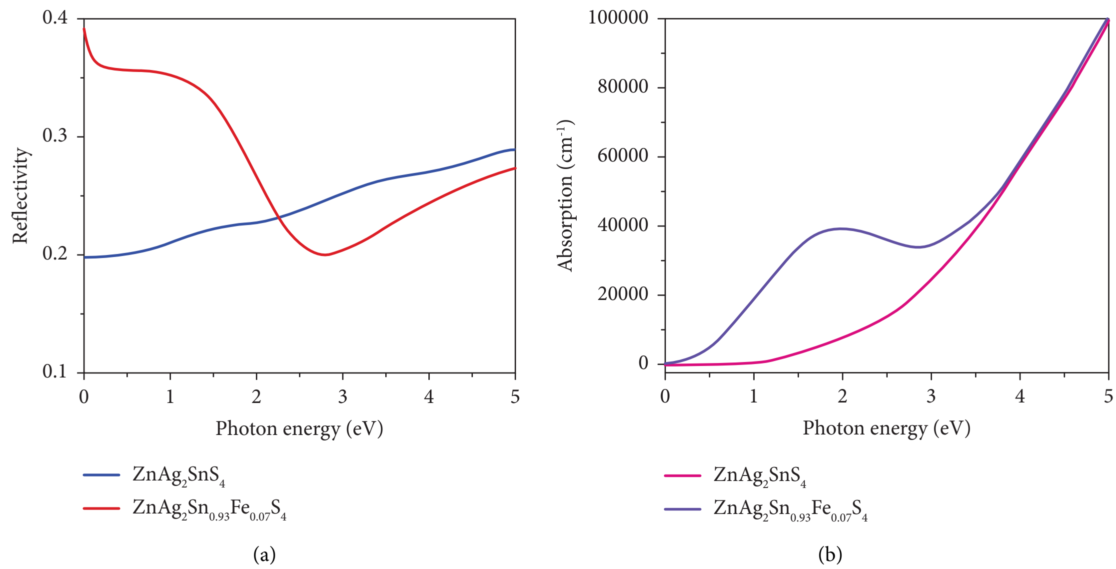

Figure 4: (a) Reflectivity for $ZnAg_2SnS_4$ and $ZnAg_2Sn_{0.93}Fe_{0.07}S_4$ and (b) absorption for $ZnAg_2SnS_4$ and $ZnAg_2Sn_{0.93}Fe_{0.07}S_4$.

through the material. In previous exploration, it was shown that a higher refractive index is associated with a larger and denser medium of material. Additionally, higher refractive index values meant that more light was slowed down as a result of being bent or refracted to a greater extent. It can be expressed in the following expression:

$$n = \frac{c}{v}, \quad (2)$$

where c represent the speed of light in vaccum and v represent the speed of light in another medium. The refractive index has two portions, namely, the real part, which indicates the phase velocity, and the imaginary part, which indicates the mass attenuation coefficient. The comparative study of refractive index as a function of photon energy for $ZnAg_2SnS_4$ and $ZnAg_2Sn_{0.93}Fe_{0.0.07}S_4$ is illustrated in Figure 5(a). The magnitudes of the refractive index for the real part are significantly higher at the initial state, while the imaginary part is reported to be almost zero for both doped and undoped. After that, the real part of $ZnAg_2Sn_{0.93}Fe_{0.0.07}S_4$ declined moderately and $ZnAg_2SnS_4$ increased slowly, whereas the imaginary part of $ZnAg_2Sn_{0.93}Fe_{0.0.07}S_4$ increased gradually at 2.5 eV. After 3 eV, however, both materials increased in a similar trend.

3.6.4. Dielectric Function. Some of the optical properties, including reflectivity, refractive index, and absorption spectrum, have been investigated by dielectric function or relative permittivity, which describes the response of a material to the application of an alternating electric field to a solid material.

$$\varepsilon = \varepsilon_1(\omega) + i\varepsilon_2(\omega). \quad (3)$$

Here, $\varepsilon_1(\omega)$ and $\varepsilon_2(\omega)$ denote the dielectric constant (real part) and the dielectric loss factor (imaginary part), respectively. The probability of photon absorption for the band structure of any material is closely related to the imaginary portion of the dielectric function. The real part of the dielectric constant maintains the energy storage potential in the electric field, while the imaginary segment indicates the opposite; even this is true for electric potential energy. From Figure 5(b), we can see that the real portion is always higher than the imaginary part within the energy range from 4.3 eV to 5 eV, where the imaginary part shows a higher value than the real portion for both doped and undoped. At the Fermi energy level, the value of the real part of $ZnAg_2SnS_4$ is reported at around 2.6, while after 7% of Fe atom doping, its value increased by 4.3 for $ZnAg_2Sn_{0.93}Fe_{0.0.07}S_4$, but the values of the imaginary part of doped and undoped crystals are accounted for almost zero.

3.6.5. Conductivity. The conduction process of photocatalytic semiconductors takes place on the basis of the energy band and free electrons, which are closely related to the discrete space of orbital electrons. It is also produced owing to the presence of free electrons and holes and the transition of free electrons from the valence band to the conduction band in the crystal materials. Optical conductivity has two segments, first, the real part, and second, the imaginary part. The real part of conductivity attains the same information as the imaginary part of the dielectric function, which describes the convective current, and the imaginary part of conductivity indicates the displacement current. Figure 6(a) depicts the comparative study of the conductivity values of doped and undoped crystals. The conductivity values of both real and imaginary parts start from almost zero at 0.0 eV. The real part of conductivity increased with a similar trend for both $ZnAg_2SnS_4$ and $ZnAg_2Sn_{0.93}Fe_{0.0.07}S_4$ in the energy range from 3 eV to 5 eV and reached 4, but the conductivity value of $ZnAg_2Sn_{0.93}Fe_{0.0.07}S_4$ within the energy range of 3 eV is higher than $ZnAg_2SnS_4$. On the other hand, the imaginary

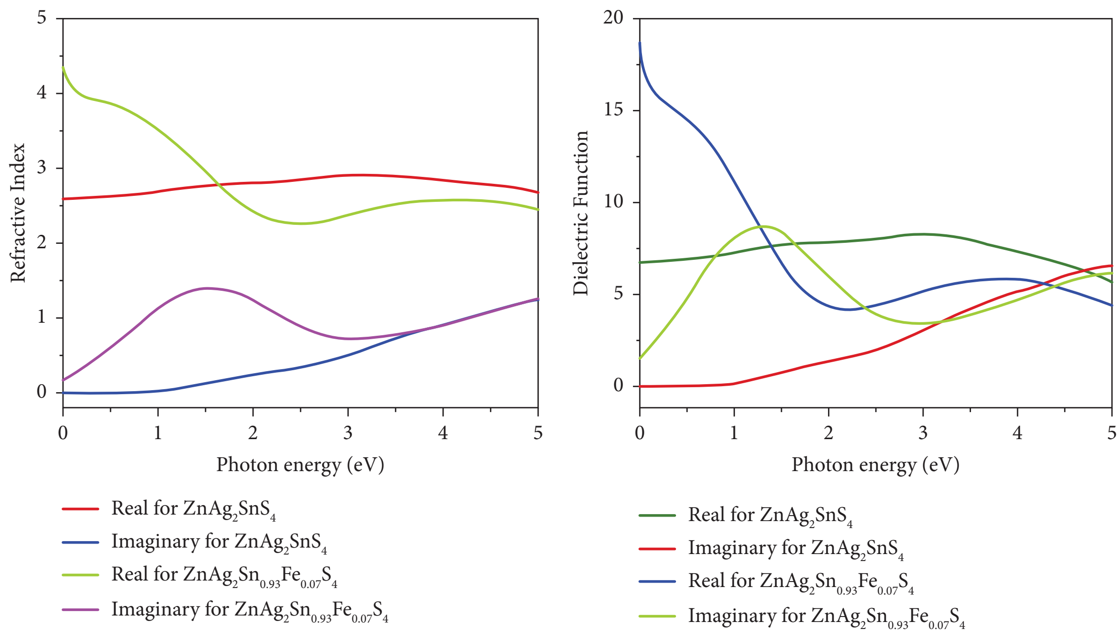

(a) (b)

FIGURE 5: (a) Refractive index for $ZnAg_2SnS_4$ and $ZnAg_2Sn_{0.93}Fe_{0.07}S_4$ and (b) dielectric function for $ZnAg_2SnS_4$ and $ZnAg_2Sn_{0.93}Fe_{0.07}S_4$.

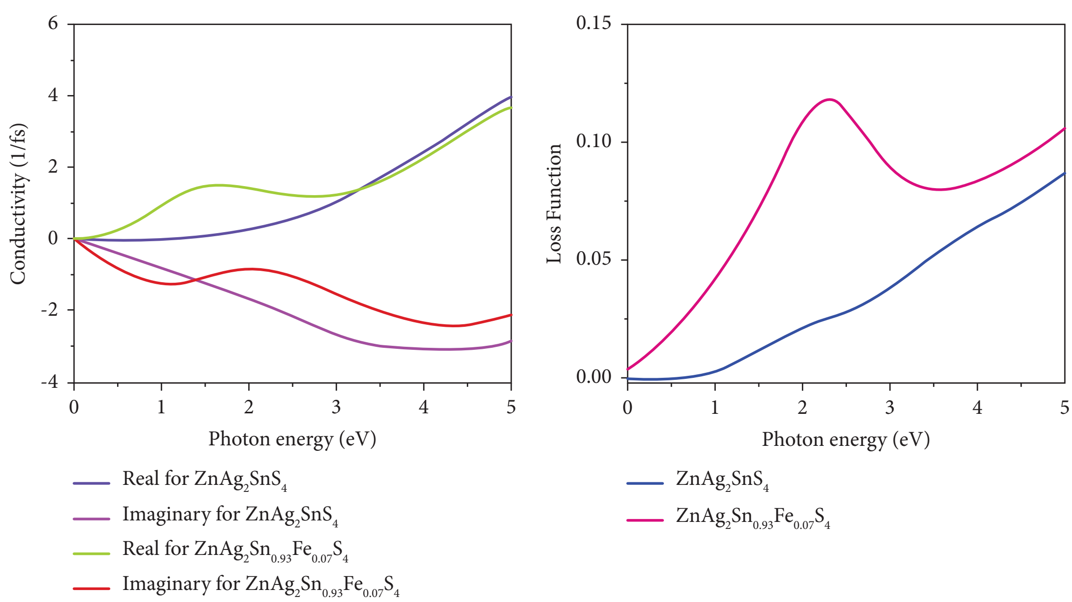

(a) (b)

FIGURE 6: (a) Conductivity for $ZnAg_2SnS_4$ and $ZnAg_2Sn_{0.93}Fe_{0.07}S_4$ and (b) loss function for $ZnAg_2SnS_4$ and $ZnAg_2Sn_{0.93}Fe_{0.07}S_4$.

part values of $ZnAg_2SnS_4$ and $ZnAg_2Sn_{0.93}Fe_{0.0.07}S_4$ went down gradually after the Fermi energy and reached −2 at 5 eV.

3.6.6. Loss Function. The loss function is a fundamental aspect of optical characteristics and consists of two photon energy zones for crystal materials. Inside the dielectric theory validation range, the energy loss function is strongly aligned with the photocatalyst dielectric function. The dielectric function reflects the response of a semiconductor to an external electromagnetic perturbation. This response is accounted for in the energy loss function. The calculated exploration of loss function values for $ZnAg_2SnS_4$ and $ZnAg_2Sn_{0.93}Fe_{0.07}S_4$ is illustrated in Figure 6. It can be observed that the loss function of $ZnAg_2Sn_{0.93}Fe_{0.07}S_4$ increased rapidly from 0 eV to 2.5 eV and peaked at 0.125 due to the splitting of the orbital. After 2.5 eV, it fell down again.

On the other hand, the loss function value for 7% doped Fe atom material increased gradually and reached by 0.075 at 5 eV.

4. Conclusion

Overall, first-principle calculations using a suitable DFT functional have been used to explore the elastic, electronic, structural, mechanical, and optical properties of the stannite type quarterly crystals of $ZnAg_2SnS_4$ and $ZnAg_2Sn_{0.93}Fe_{0.07}S_4$. The Mulliken bond population analysis, which reveals the bonding nature of Zn-S, Ag-S, S-Sn, S-Sn, and Fe-S was calculated and used to investigate the obtained lattice parameters value and chemical bonding of $ZnAg_2SnS_4$ and $ZnAg_2Sn_{0.93}Fe_{0.07}S_4$ and confirmed the optimized structures. Secondly, the calculated band gaps of $ZnAg_2GeS_4$, $ZnAg_2SnS_4$, and $ZnAg_2Sn_{0.93}Fe_{0.07}S_4$ were found at 0.93 eV, 1.15 eV, and 0.32 eV, respectively, using GGA with PBE function. In addition, the experimental band gap of the $ZnAg_2GeS_4$ is 0.94 eV that is almost same to the calculated band gap (0.93 eV) in this study which indicates the accuracy of this study for all crystals. Another objective of this study is the doping on $ZnAg_2SnS_4$ by the most available metals replacing Sn, where 7% Fe atoms were doped and found a very lower band gap, 0.32 eV, indicating the material is well-suited for absorbing all UV or visible light in the higher wavelength region and displaying enhanced photocatalyst performance in comparison to the $ZnAg_2SnS_4$ crystal. The extension for the other properties of designed crystals were evaluated by mechanical and elastic properties, which have shown to be ductile, stiffer, and anisotropic, indicating that both semiconductors-based photocatalysts are ductile. The mechanical and elastic properties have been shown to be ductile, stiffer, and anisotropic, indicating that both semiconductors are ductile. To foretell efficient semiconduction in photocatalysts, we have computed their optical properties such as reflectivity, absorption, refractive index, dielectric function, conductivity, and loss function. For Fe doped of $ZnAg_2Sn_{0.93}Fe_{0.07}S_4$, with its increased absorption spectrum in the UV visible region, it is found to be superior to $ZnAg_2SnS_4$ as a photocatalyst for use in waste water treatment. Therefore, it is evident to conclude that semiconductor-based $ZnAg_2Sn_{0.93}Fe_{0.07}S_4$, after being doped with 7% Fe atoms, has enhanced photocatalytic performance to that of undoped $ZnAg_2SnS_4$.

Data Availability

The data used to support the findings of this study are available from the corresponding author upon request.

Conflicts of Interest

The authors declare that they have no conflicts of interest.

References

[1] K. M. Lee, C. W. Lai, K. S. Ngai, and J. C. Juan, "Recent developments of zinc oxide based photocatalyst in water treatment technology: a review," *Water Research*, vol. 88, pp. 428–448, 2016.

[2] M. Hobday, "Innovation in asian industrialization: a gerschenkronian perspective," *Oxford Development Studies*, vol. 31, no. 3, pp. 293–314, 2003.

[3] R. Jenkins, "The political economy of industrialization: a comparison of Latin American and East Asian newly industrializing countries," *Development and Change*, vol. 22, no. 2, pp. 197–231, 1991.

[4] P. Westerhoff, T. Boyer, and K. Linden, "Emerging water technologies: global pressures force innovation toward drinking water availability and quality," *Accounts of Chemical Research*, vol. 52, no. 5, pp. 1146-1147, 2019.

[5] H. Escobar, *Brazilian President Attacks Deforestation Data*, American Association for the Advancement of Science, Washington, DC, USA, 2019.

[6] N. Hosonuma, M. Herold, V. De Sy et al., "An assessment of deforestation and forest degradation drivers in developing countries," *Environmental Research Letters*, vol. 7, no. 4, Article ID 044009, 2012.

[7] S. N. Sakthivel, B. Neppolian, M. V. Shankar, B. Arabindoo, M. Palanichamy, and V. Murugesan, "Solar photocatalytic degradation of azo dye: comparison of photocatalytic efficiency of ZnO and TiO2," *Solar Energy Materials and Solar Cells*, vol. 77, no. 1, pp. 65–82, 2003.

[8] G. Z. Li, W. Zhang, J. Hou et al., "Enhanced visible light photochemical activity and stability of MoS_2/Cu_2O nanocomposites by tunable heterojunction," *Materials Today Communications*, vol. 23, Article ID 100933, 2020.

[9] M. Wen, J. Wang, R. Tong et al., "A low-cost metal-free photocatalyst based on black phosphorus," *Advanced Science*, vol. 6, no. 1, Article ID 1801321, 2019.

[10] H. Zhao, S. Sun, P. Jiang, and Z. J. Xu, "Graphitic C3N4 modified by Ni2P cocatalyst: an efficient, robust and low cost photocatalyst for visible-light-driven H2 evolution from water," *Chemical Engineering Journal*, vol. 315, pp. 296–303, 2017.

[11] K. Hakobyan, T. Gegenhuber, C. S. P. McErlean, and M. Müllner, "Visible-light-driven MADIX polymerisation via a reusable, low-cost, and non-toxic bismuth oxide photocatalyst," *Angewandte Chemie International Edition*, vol. 58, no. 6, pp. 1828–1832, 2019.

[12] H. Y. Hafeez, S. K. Lakhera, N. Narayanan et al., "Environmentally sustainable synthesis of a CoFe2O4–TiO2/rGO ternary photocatalyst: a highly efficient and stable photocatalyst for high production of hydrogen (solar fuel)," *ACS Omega*, vol. 4, no. 1, pp. 880–891, 2019.

[13] T. Sinha, M. Ahmaruzzaman, P. P. Adhikari, and R. Bora, "Green and environmentally sustainable fabrication of Ag-SnO2 nanocomposite and its multifunctional efficacy as photocatalyst and antibacterial and antioxidant agent," *ACS Sustainable Chemistry & Engineering*, vol. 5, no. 6, pp. 4645–4655, 2017.

[14] R. Liu, P. Wang, X. Wang, H. Yu, and J. Yu, "UV-and visible-light photocatalytic activity of simultaneously deposited and doped Ag/Ag (I)-TiO2 photocatalyst," *Journal of Physical Chemistry C*, vol. 116, no. 33, pp. 17721–17728, 2012.

[15] M. I. Ali, M. Jahidul, M. Rafid et al., "The computational screening of structural, electronic, and optical properties for SiC, $Si_{0.94}Sn_{0.06}C$, and $Si_{0.88}Sn_{0.12}C$ lead-free photovoltaic inverters using DFT functional of first principle approach," *Eurasian Chemical Communications*, vol. 3, no. 5, pp. 327–338, 2021.

[16] M. S. H. Tomal Hossain and M. Hazrat Ali, "Unesco chakma, ajoy kumer, Mohammad Jahidul Islam;, Investigation of optoelectronics, thermoelectric, Structural and photovoltaic

Properties of $CH_3NH_3SnBr_3$ lead-free organic perovskites," *Chemical Methodologies*, vol. 5, pp. 259–270, 2021.
[17] A. Kumer and U. Chakma, "Developing the amazing photocatalyst of $ZnAg_2GeSe_4$, $ZnAg_2Ge_{0.93}Fe_{0.07}Se_4$ and $ZnAg_{2\text{-}}Ge_{0.8}6Fe_{0.14}Se_4$ through the computational explorations by four DFT functionals," *Heliyon*, vol. 7, no. 7, 2021.
[18] U. Chakma, A. Kumer, K. B. Chakma, M. T. Islam, D. Howlader, and R. M. K. Mohamed, "Electronics structure and optical properties of $SrPbO_3$ and $SrPb_{0.94}Fe_{0.06}O_3$: a first principle approach," *Eurasian Chemical Communications*, vol. 2, no. 5, pp. 573–580, 2020.
[19] U. Chakma, A. Kumer, K. B. Chakma, M. T. Islam, and D. Howlader, "Electronics Structure and optical Properties of Ag_2BiO_3,$(Ag_2)_{0.88}Fe_{0.12}BiO_3$: a first principle approach," *Advanced Journal of Chemistry-Section A*, vol. 3, no. 4, pp. 542–550, 2020.
[20] B. C. Kamal, K. Ajoy, C. Unesco, H. Debashis, and M. T. Islam, "A theoretical investigation for electronics structure of $Mg(BiO_2)_2$ semiconductor using first principle approach," *International Journal of Networks and Communications*, vol. 7, no. 3, pp. 247–255, 2020.
[21] M. T. Islam, A. Kumer, U. Chakma, and D. Howlader, "A computational Investigation of electronic Structure and optical Properties of $AlCuO_2$ and $AlCu_{0.96}Fe_{0.04}O_2$: a first principle approach," *Orbital-The Electronic Journal of Chemistry*, vol. 13, no. 1, 2021.
[22] M. B. Ahmed, A. Kumer, M. Islam, and T. S. A. Islam, "The photochemical degradation (PCD) of nitrobenzene (NB) using UV light and fenton reagent under various conditions," *Journal of the Turkish Chemical Society, Section A: Chemistry*, vol. 5, no. 2, pp. 803–818, 2018.
[23] S. Ma Mokit, U. Chakma, A. Kumer, M. J. Islam, A. Habib, and M. M. Alam, "The Exploration of structural, Electronic and optical Properties for MoS_2 and $Mo_{0.95}W_{0.05}S_2$ photocatalyst Effort on wastewater Treatment using DFT Functional of first principle approach," *Applied Journal of Environmental Engineering Science*, vol. 7, no. 1, pp. 103–113, 2021.
[24] M. J. Islam and A. Kumer, "First-principles study of structural, electronic and optical properties of $AgSbO_3$ and $AgSb_{0.78}Se_{0.22}O_3$ photocatalyst," *SN Applied Sciences*, vol. 2, no. 2, p. 251, 2020.
[25] M. M. Hasan, K. Ajoy, and U. Chakma, "Theoretical Investigation of doping Effect of Fe for $SnWO_4$ in electronic Structure and optical properties: DFT based first principle study," *Advanced Journal of Chemistry-Section A*, vol. 03, no. 5, pp. 639–644, 2020.
[26] M. M. Hasan, A. U. Kumer, U. Chakma, and M. T. Islam, "Structural, optical and electronic properties of $ZnAg_2GeTe_4$ and $ZnAg_2Ge_{0.93}Fe_{0.07}Te_4$ Photocatalyst: a first principle approach," *Molecular Simulation*, vol. 47, no. 7, pp. 594–601, 2021.
[27] M. Ali, M. J. Islam, A. Kumer et al., "Investigation of structural, electronic and optical properties of Na 2 InAgCl 6, K 2 InAgCl 6, and Rb 2 InAgCl 6 lead-free halide double perovskites regarding with Cs 2 InAgCl 6 perovskites cell and a comparative study by DFT functionals," *Materials Research*, vol. 24, 2021.
[28] U. Chakma, "Investigation of electronic structure, optical properties, map of electrostatic potential, and toxicity of Hfo2, Hf0. 88si0. 12o2, Hf0. 88Ge0. 12o2 and Hf0. 88Sn0. 12O2 by computational and virtual screening," *Journal of Computational Electronics*, vol. 22, no. 1, pp. 1–16, 2023.
[29] K. A. Hoque, A. Kumer, U. Chakma, and A. N. Chowdury, "Facile synthesis of computationally designed MgAl2O4/CeO2/Cu2o and MgAl2O4/CeO2/Ag2o smart heterojunction photocatalysts for aqueous organic pollutants degradation," *ECS Transactions*, vol. 107, no. 1, pp. 13785–13796, 2022.
[30] S. Khatun, A. Kumer, C. K. Roy, M. Moniruzzaman, and A. N. Chowdury, "Fabrication of cellulose capped MnxOy-Ag nanocomposites and investigation of its oxidative and antibacterial efficacy in water environment," *ECS Transactions*, vol. 107, no. 1, pp. 15817–15824, 2022.
[31] A. Kumer, U. Chakma, M. M. Alam et al., "Structural, electronic, and opto-electronic properties for BiVS4 photocatalyst effort on wastewater treatment with comparison a standard photocatalyst BiVO4 through the first principles," *ECS Transactions*, vol. 107, no. 1, pp. 12109–12119, 2022.
[32] A. Alzamly, F. Hamed, T. Ramachandran et al., "Tunable band gap of Bi3+-doped anatase TiO2 for enhanced photocatalytic removal of acetaminophen under UV-visible light irradiation," *Journal of Water Reuse and Desalination*, vol. 9, no. 1, pp. 31–46, 2019.
[33] R. RameshKumar, T. Ramachandran, K. Natarajan, M. Muralidharan, F. Hamed, and V. Kurapati, "Fraction of rare-earth (Sm/Nd)-lanthanum ferrite-based perovskite ferroelectric and magnetic nanopowders," *Journal of Electronic Materials*, vol. 48, no. 3, pp. 1694–1703, 2019.
[34] J. Bennet, R. Tholkappiyan, K. Vishista, N. V. Jaya, and F. Hamed, "Attestation in self-propagating combustion approach of spinel AFe2O4 (A= Co, Mg and Mn) complexes bearing mixed oxidation states: magnetostructural properties," *Applied Surface Science*, vol. 383, pp. 113–125, 2016.
[35] R. K. Raji, T. Ramachandran, M. Muralidharan et al., "Twitching the inherent properties: the impact of transition metal Mn-doped on LaFeO 3-based perovskite materials," *Journal of Materials Science: Materials in Electronics*, vol. 32, no. 20, pp. 25528–25544, 2021.
[36] R. Tholkappiyan and K. Vishista, "Structural, optical and magnetic properties of nanocrystalline zinc ferrite particles from glycine assisted combustion: effect of Sr2+ dopant," *International Journal of Materials Research*, vol. 106, no. 2, pp. 127–136, 2021.
[37] T. O. Sasamura, T. Osaki, T. Kameyama et al., "Solution-phase synthesis of stannite-type Ag2ZnSnS4 nanoparticles for application to photoelectrode materials," *Chemistry Letters*, vol. 41, no. 9, pp. 1009–1011, 2012.
[38] Y. Shapira, E. J. McNiff, N. F. Oliveira, E. D. Honig, K. Dwight, and A. Wold, "Magnetic properties of Cu 2 Zn 1− x Mn x GeS 4: antiferromagnetic interactions in the wurtz-stannite structure," *Physical Review B*, vol. 37, no. 1, pp. 411–418, 1988.
[39] M. M. Alam, U. Chakma, A. Kumer et al., "Investigation of structural, electronic, and optical properties of CdAg2GeSe4 and HgAg2GeSe4 amazing photocatalyst regarding with ZnAg2GeSe4 and a comparative study by DFT functionals," *ECS Transactions*, vol. 107, no. 1, pp. 15375–15385, 2022.
[40] H. Katagiri, "Cu_2ZnSnS_4 thin film solar cells," *Thin Solid Films*, vol. 480-481, pp. 426–432, 2005.
[41] A. A., R. Nagoya, R. Asahi, and G. Kresse, "First-principles study of Cu_2ZnSnS_4 and the related band offsets for photovoltaic applications," *Journal of Physics: Condensed Matter*, vol. 23, no. 40, Article ID 404203, 2011.
[42] P. K. Sarswat and M. L. Free, "A study of energy band gap versus temperature for Cu_2ZnSnS_4 thin films," *Physica B: Condensed Matter*, vol. 407, no. 1, pp. 108–111, 2012.
[43] J. J. Scragg, P. J. Dale, L. M. Peter, G. Zoppi, and I. Forbes, "New routes to sustainable photovoltaics: evaluation of Cu2ZnSnS4 as an alternative absorber material," *Physica Status Solidi (B)*, vol. 245, no. 9, pp. 1772–1778, 2008.

[44] J. S. L. Seol, S. Lee, J. C. Lee, H. D. Nam, and K. H. Kim, "Electrical and optical properties of Cu_2ZnSnS_4 thin films prepared by rf magnetron sputtering process," *Solar Energy Materials and Solar Cells*, vol. 75, no. 1-2, pp. 155–162, 2003.
[45] P. K. Ziesche, S. Kurth, and J. P. Perdew, "Density functionals from LDA to GGA," *Computational Materials Science*, vol. 11, no. 2, pp. 122–127, 1998.
[46] M. D. Segall, P. J. D. Lindan, M. J. Probert et al., "First-principles simulation: ideas, illustrations and the CASTEP code," *Journal of Physics: Condensed Matter*, vol. 14, no. 11, pp. 2717–2744, 2002.
[47] J. Ramos, "Introducción a Materials Studio en la Investigación Química y Ciencias de los Materiales," 2020, http://hdl.handle.net/10261/207598.
[48] A. Kumer, M. N. Sarker, and S. Paul, "HyperChem programı kullanarak bazı aromatik karboksilik asitlerin HOMO, LUMO, termoplastik özellikleri ve QSAR incelemesinin teorik araştırılması," *International Journal of Chemistry and Technology*, vol. 3, no. 1, pp. 26–37, 2019.
[49] A. Kumer, M. N. Sarker, S. Paul, and A. Zannat, "The theoretical prediction of thermophysical properties, HOMO, LUMO, QSAR and biological indics of cannabinoids (CBD) and tetrahhdrocannabinol (THC) by computational chemistry," *Advanced Journal of Chemistry-Section A*, vol. 2, no. 3, pp. 190–202, 2019.
[50] A. Kumer, M. N. Sarker, and S. Paul, "The thermo physical, HOMO, LUMO, Vibrational spectroscopy and QSAR study of morphonium formate and acetate Ionic Liquid Salts using computational method," *Turkish Computational and Theoretical Chemistry*, vol. 3, no. 2, pp. 59–68, 2019.
[51] A. Kumer, M. N. Sarkar, and S. Pual, "The simulating study of HOMO, LUMO, thermo physical and quantitative structure of activity relationship (QSAR) of some anticancer active ionic liquids," *Eurasian Journal of Environmental Research*, vol. 3, no. 3, pp. 1–10, 2019.
[52] K. Li, B. Chai, T. Peng, J. Mao, and L. Zan, "Synthesis of multicomponent sulfide Ag 2 ZnSnS 4 as an efficient photocatalyst for H 2 production under visible light irradiation," *RSC Advances*, vol. 3, no. 1, pp. 253–258, 2013.
[53] B. Ghebouli, M. Ghebouli, M. Fatmi, and A. Bouhemadou, "First-principles study of the structural, elastic, electronic, optical and thermodynamic properties of the cubic perovskite CsCdCl3 under high pressure," *Solid State Communications*, vol. 150, no. 39-40, pp. 1896–1901, 2010.
[54] K. Panda and K. Ravi Chandran, "Determination of elastic constants of titanium diboride (TiB2) from first principles using FLAPW implementation of the density functional theory," *Computational Materials Science*, vol. 35, no. 2, pp. 134–150, 2006.
[55] P. Ravindran, L. Fast, P. A. Korzhavyi, B. Johansson, J. Wills, and O. Eriksson, "Density functional theory for calculation of elastic properties of orthorhombic crystals: application to TiSi 2," *Journal of Applied Physics*, vol. 84, no. 9, pp. 4891–4904, 1998.